Delivering the 3b generation of LNMO cells for the xEV market of 2025 and beyond

Material degradation study

Horizon 2020 | LC-BAT-5-2019
Research and innovation for advanced Li-ion cells (generation 3b)
GA # 875033

Deliverable No.	D2.3	
Deliverable Title	Final material data report and definition of final 3beLiEVe cell chemistry	
Deliverable Type	Report	
Dissemination level	Public	
Written By	Marcus Fehse, Marta Cabello (CICe); Marie Bichon (Arkema)	08-2022
Checked by	Damian Cupid (AIT)	03-10-2022
Approved by	Boschidar Ganev (AIT)	27-10-2022
Status	Final	27-10-2022

This project has received funding from the European Union's H2020 research and innovation programme under Grant Agreement no. 875033.

Revision History

Version	Date	Who	Changes
1	20/01/2022	Marcus Fehse	Initial draft for internal review
2	25/05/2022	Marcus Fehse	Complementation with results of final cell chemistry
3	26/07/2022	Marcus Fehse	Amendments of third-party contributions CRF, ARK
4	17/08/2022	Marta Cabello	Include insights from full cell analysis at CICe
5	02/09/2022	Boschidar Ganev	Basic formatting and cleanup for readability
5	03/10/2022	Damian Cupid	Content review
6	17/10/2022	Marcus Fehse	Updates in response to revision request: Executive Summary updated; section 2 updated; section 3.4 updated; added new section 3.6; section 4 and 4.1 updated; section 5 updated (added final sentence in first paragraph). Section 6 (conclusions) was updated; List of acronyms has been updated.
6	27/10/2022	Boschidar Ganev	Final editorial and formatting.

Project Abstract

3beLiEVe aims to strengthen the position of the European battery and automotive industry in the future xEV market by delivering the next generation of battery cells, designed and made in Europe, for the electrified vehicles market of 2025 and beyond. The project activities are focused on three domains:

- Development of automotive battery cells that are highly performant (high energy density, fast charge capability, long cycle life) and free of critical raw materials such as cobalt and natural graphite;
- Development and integration of sensors into and onto the cells to enable smart, adaptive operating strategies and advanced diagnostics in order to extend the useful life of the battery in first and second life applications and improve safety;
- A comprehensive manufacturing approach that is designed from the outset for a circular economy and industrial volumes. This encompasses green manufacturing processes for cell, module and pack, as well as recyclability assessment of the components, and a target lifecycle cost of 90 €/kWh at scale.

The project will deliver two 12kWh-demonstrator battery packs at TRL6 and MRL8. These aim at demonstrating the 3beLiEVe technology performance for applications in light duty (i.e. passenger cars, freight vehicles) and commercial vehicles (i.e. city buses and trucks) in fully electric/plug-in hybrid (BEV/PHEV) configurations.

The strong and complementary consortium of 21 partners from 10 different European countries representing industrial companies, SMEs, RTOs and academia is coordinated by AIT Austrian Institute of Technology. 3beLiEVe is scheduled to run from January 1st, 2020 to June 30th, 2023, for a total duration of 42 months and has received funding from the European Union's H2020 research and innovation programme under Grant Agreement no. 875033. A full list of partners and funding can be found at: https://cordis.europa.eu/project/id/875033.

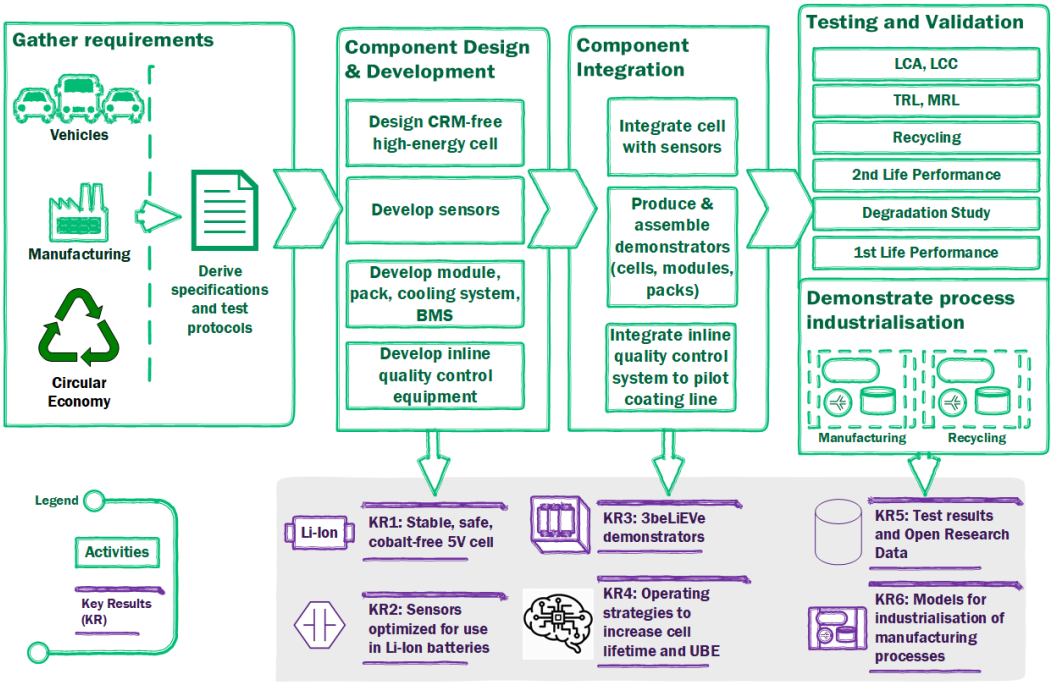

Figure 1. Overview of major 3beLiEVe project steps.

Executive Summary

This deliverable is the outcome of T2.4 and provides an overview of the diverse characterization techniques applied to elucidate material degradation process on half cell and full cell levels using the final 3beLiEVe cell chemistry. Cathode candidate LNMO4 reveals good structural stability although electrode cross-talk has been observed. Anode graphite Si/C composite undergoes strong morphological changes upon cycling as well as considerable capacity loss.

At full cell level, the loss of cyclable Li inventory was confirmed and identified as one of the main drivers of capacity loss. Relative to its original due date, this document is issued with a delay of several months arising from the delay of final cell chemistry as described in *D2.2 Final material data report and definition of final 3beLiEVe cell chemistry*. Due to the excess in workload and the resulting delay not all the tests that were originally foreseen could be carried out at full cell level. The analysis of degradation mechanisms and phenomena, as well as testing with automotive cycles, will be continued in task T7.1 at 30Ah cell level and documented in public deliverable *D7.1 Test report on prototype cells including baseline data*.

Table of Contents

List of figure and tables

List of abbreviations

Acronym / Short Name	Meaning
AM	Active material
BOL	Begin of Life
BSE	Back scattered electron
CB	Carbon black
CC	Constant current
CE	Coulombic Efficiency
CMC	Carboxymethyl cellulose
CNT	Carbon nanotubes
CV	Constant voltage
DMC	Dimethyl carbonate
DOD	Depth of discharge
EIS	Electrochemical Impedance Spectroscopy
EMC	Ethyl methyl carbonate
EOC	End of charge
EOD	End of discharge
FEC	Fluoroethylene carbonate
GC-MS	Gas chromatography mass spectroscopy
HVE	High Voltage Electrolyte
ICE	Initial Coulombic Efficiency
LiFSI	Lithium bis(fluorosulfonyl)imide
LNMO	$LiNi_{0.5}Mn_{1.5}O_4$
NMP	N-Methyl-2-pyrrolidone
NPD	Neutron powder diffraction
PVDF	Polyvinylidene fluoride
SBR	Styrene-butadiene rubber
Si/C	Si/graphite composite
SOC	State of charge
TM(s)	Transition metal(s)
XRD	X-Ray diffraction

1. Introduction

The main objective of the study summarized in this deliverable and carried out within task T2.4 of the 3beLiEVe project was to investigate the reversible and irreversible processes that the battery components (anode, electrolyte, cathode) undergo upon electrochemical cycling. Particularly, the study of irreversible processes is of great interest as they play a pivotal role in material degradation and lead to performance decay, as previously documented in *D2.2 Final material data report and definition of final 3beLiEVe cell chemistry*. In the present document, we strive to elucidate their origin and identify the principal drivers of performance decrease during cycle life.

2. Overview of degradational analysis performed

A battery is a closed system in which the structural, compositional, and morphological changes of its main components (cathode, anode, electrolyte) cannot be directly observed. Within this study, a multitude of characterization techniques were employed to comprehensively investigate and characterize these material-based transformations. The measurements were conducted under different conditions; i) measurements of cycled electrodes from disassembled cells (ex situ), ii) measurements in battery like configurations (in situ), and iii) acquiring characterization data while the battery is subjected to electrochemical cycling (operando). An overview of the diverse characterization techniques and the mode of data acquisition is given in Table 1.

Table 1 Characterization techniques applied to different cell types for investigation of degradation behaviour. Under different acquisition conditions; x = ex situ, i = in situ; o = operando.

Active materials / Technique	**Half cell**			**Full cell**	
	LNMO vs Li	**Graphite vs Li**	**Si/C vs Li**	**LNMO vs Graphite**	**LNMO vs Si/C**
(FIB) SEM	x	x	x	x	(x)
Raman	x	x	x		x
EIS	i			x	
XPS	x			x	
XAS	o				x
XRD	o, x				
NPD	o, x				
GC-MS				x	x
Visual inspection	x	x	x	x	x

3. Degradational analysis on LNMO half cells

General remarks: All cells described in this section were built in coin cell format with LNMO as the cathode and Li metal as the counter electrode using LP30 electrolyte. As described in previous deliverables *D2.1 Preliminary material data report (electrode components and processing)* and *D2.2 Final material data report and definition of final 3beLiEVe cell chemistry*, the selected high voltage electrolyte (HVE) is not compatible with a stainless-steel environment. The cells were subjected to electrochemical cycles as indicated in *D2.1* Table 4. The cells were opened after complete full electrochemical cycles under inert atmosphere using a coin cell disassembling tool from Hohsen Corp. Electrodes were thoroughly washed three times with DMC solvent.

3.1. SEM

Micrographs of LNMO electrode before and after pressing as well as after 123 and 844 cycles are shown in Figure 2. The micrographs reveal no sign of cracking or major particle detachment after pressing of the electrode. For the cycled electrodes a similar microstructure and particle morphology as for the pristine sample is observed, which suggests a stable electrode integrity upon electrochemical cycling. However, cracking of individual particles is detected after 844 cycles.

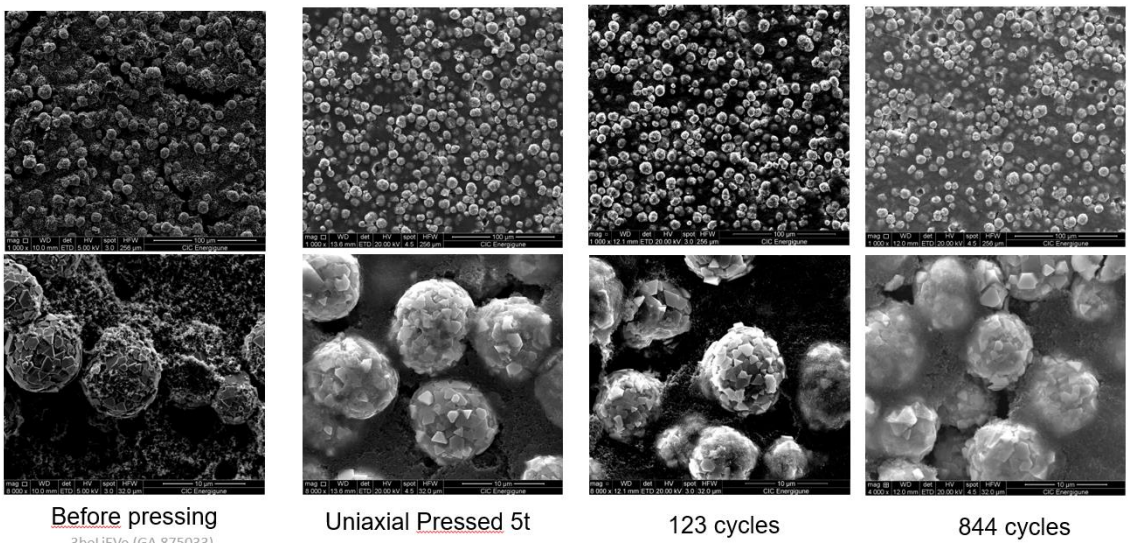

Figure 2 SEM micrographs of LNMO electrodes at two different magnifications before and after pressing as well as after 123 and 844 of electrochemical cycling vs Li metal.

3.2. Raman

In Figure 3, Raman spectra of the LNMO electrodes after 670 electrochemical cycles are compared to the spectrum of the pristine material. Both spectra coincide well with each other, revealing the main spectral features resulting from the excitation of TM—O vibrational bonds, as indicated by the arrows. Raman spectroscopy shows that the local structure of LNMO is well preserved for hundreds of cycles. No peak broadening or peak shifts are observed which would indicate particle breakdown or transformation of the chemical state of the LNMO. The later underlines the high reversibility of the electrochemical redox reaction. The features below 150 cm^{-1} for the cycled electrode are most likely related to CEI formation, although this could not be confirmed with certainty.

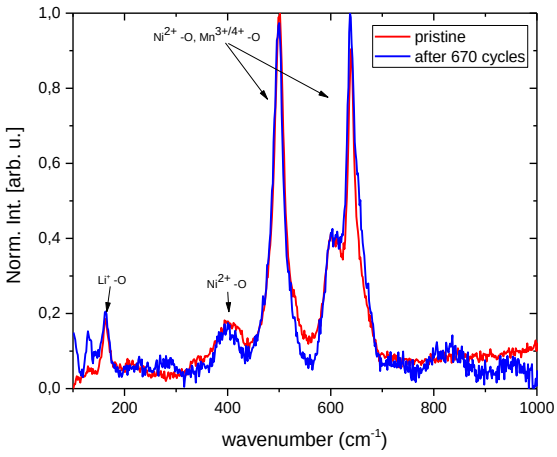

Figure 3 Raman spectra of pristine and cycled LNMO electrode vs Li metal. Arrows indicate attribution of main active vibrational bonds in the LNMO structure.

3.3. XPS

X-ray photon spectroscopy is a highly surface-sensitive spectroscopic technique that allows the elemental composition of the near-surface layer(s) of pristine and ex situ cycled electrodes to be determined. Differently from the above-described sample preparation method, we abstained from the washing step for the Li counter electrode samples in order to avoid the potential removal of deposited TM. In Figure 4 the XPS spectra acquired on a Li metal counter electrode cycled vs a LNMO cathode for 124 cycles are presented. The spectra reveal Ni 2p as well as Mn 3p peaks, which confirm the presence of both TM on the Li counter electrode. This highlights their dissolution from the cathode and shuttling to the counter electrode. Interestingly, the ratio of Ni/Mn at the Li counter electrode is approximately 1/3, which is the stoichiometry of Ni and Mn in the cathode material. This points towards an equal susceptibility of both TM to dissolve and migrate to the counter electrode during electrochemical cycling. Furthermore, we found no significant increase in TM amount deposited on counter electrode for samples cycled >800 cycles (not shown), which suggests that the dissolution and migration process does not evolve linearly with cycle number.

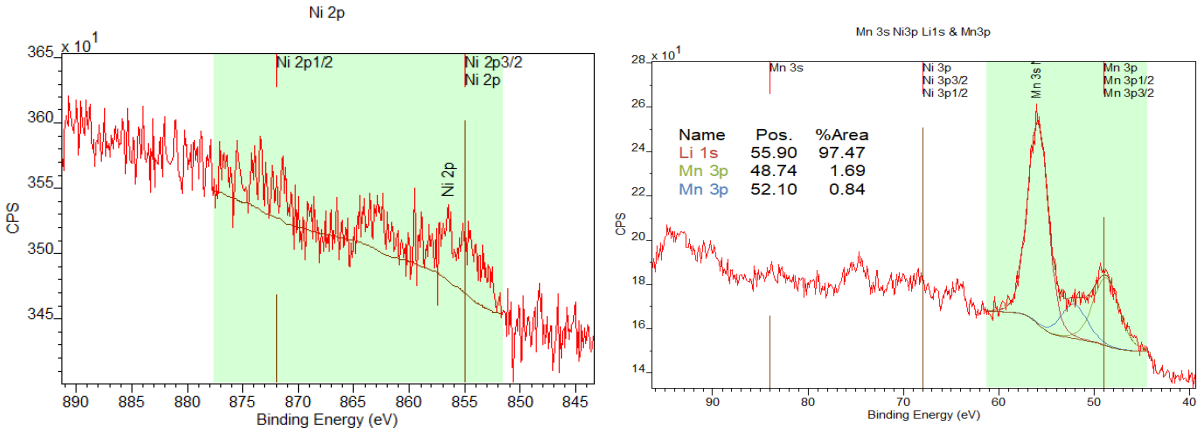

Figure 4 XPS spectra of Li counter electrode of LNMO sample cycled for 124 cycles, revealing both Ni (left) as well as Mn (right) presence.

Turning to the LNMO cathode, XPS spectra were acquired in the pristine state (red), after soaking with electrolyte without current applied (green) as well as after 124 electrochemical cycles (blue) vs Li metal. The most salient changes that we observed are for oxygen, depicted in Figure 5 (left), which presents a clear shift to higher binding energies from lattice oxygen to C=O and C-O. This suggests that the cathode surface gets covered with carbonates (and phosphates) when being wetted with electrolyte and that this proceeds during electrochemical cycling. This is also supported by a diminishing signal of the TM (not shown). Another element of interest is Fluorine, which is reflected by the F1s spectra in Figure 5 (right). The main peak is centred around 688eV, which can be attributed to the CF2-CH2 group stemming from the PVdF binder. Interestingly, no significant shift in covalent bonding nature is observed upon electrochemical cycling. The absence of ionic bound fluorine (e.g. LiF) suggest that HF attack (formed from water traces in the cell) is not the dominant parasitic reaction in this configuration.

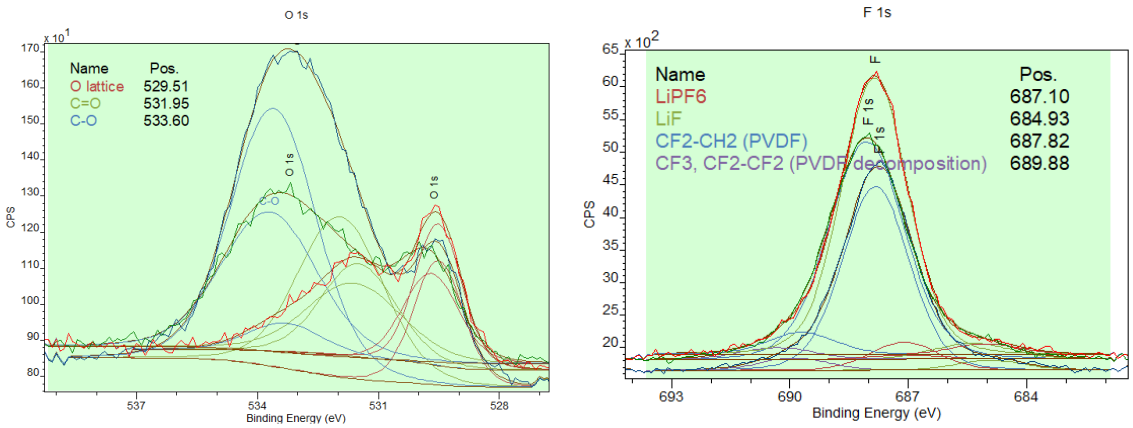

Figure 5 XPS spectra of LNMO electrode at O1s (left) and F1s (right) binding energy. Red spectra correspond to pristine, green to OCV, and blue to cycled electrode after 124

3.4. Diffraction

The XRD pattern of pristine and cycled LNMO materials are shown in Figure 6. The diffraction peaks largely coincide with each other, which confirms the preservation of the spinel phase after cycling. No additional peaks are observed which would hint at the irreversible formation or segregation of secondary crystalline phases upon electrochemical cycling. Nevertheless, a shift of the diffraction pattern to slightly higher 2θ values can be observed. By Rietveld refinement it was shown that the lattice constant of cycled LNMO is slightly smaller than that of the pristine phase. This can be attributed to the fact that Li reinsertion into LNMO was incomplete. The higher background and the broad hump at around 13° of the cycled electrode is due to the presence of amorphous additives within the electrode mix, which scatter the x-ray signal.

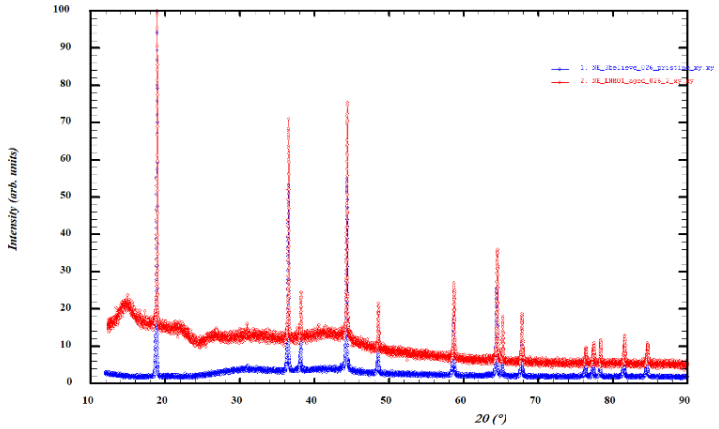

Figure 6 X-ray diffraction pattern of pristine(blue) and electrochemical cycled (red) LNMO electrode.

Similarly, neutron powder diffraction (NPD) was performed, and patterns were refined on pristine as well as *ex situ* samples at distinct points of charge as well as after several complete cycles (not shown). These patterns show the reversible contraction and expansion upon delithiation and lithiation of the LNMO host structure. Furthermore, the patterns confirm that the spinel structure is maintained, as no broadening is observed. Furthermore, the TM order is preserved upon cycling.

3.5. X-ray absorption spectroscopy

An X-ray absorption spectroscopy study was conducted on two different LNMO types; one with high level of TM- ordering ($P4_332$- phase) and one in which the TM are randomly distributed in the 16*d*-sites (*Fd*3*m*-phase) under *operando* conditions. Besides providing valuable insights on the redox activity of both TM and the differences and similarities in redox reaction and reaction kinetics between the two phases, this experiment also revealed the presence of parasitic reactions. We found that at elevated potential >4.9V vs. Li^+/Li, the applied charge current led to no more oxidation state changes of the TMs, which is depicted in Figure 7, highlighted in the dashed rectangular. This infers that the provided electrons are consumed in parasitic oxidative reactions such as electrolyte decomposition and are lost for subsequent discharge. Although parasitic oxidative reactions are a well-known phenomenon, this operando XAS study is capable of visualizing them directly. For more information on this study, we refer the interested reader to the publication https://doi.org/10.1021/acs.chemmater.2c01360 .

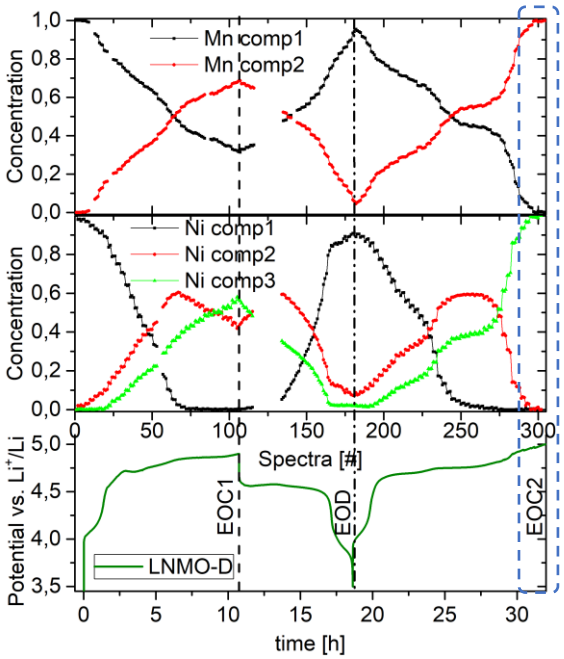

Figure 7 Evolution of Mn and Ni components which correspond to the $Mn^{3+/4+}$ and the $Ni^{2+/3+/4+}$ phases upon charge, discharge and 2nd charge for TM disordered LNMO sample. The dashed rectangular highlights the region at elevated oxidation potential in 2nd charge at which charge current is decoupled from oxidation state changes.

3.6. Electrochemical cycling at high rates and elevated temperature

To evaluate the influence of temperature on rate capability and capacity retention of LNMO cathode material, half-cell coin cells of the selected LNMO4 candidate were prepared and cycled under room temperature and 55ºC. While similar reversible capacities were obtained during the first cycles (formation) it is salient that the initial coulombic efficiency (ICE) was lower at elevated temperature compared to RT (78% vs 93%), which suggests increased parasitic reaction. Upon increase of cycling rate from C/5 to 3C (rate capability test) the cell at elevated temperature shows higher capacity values than the RT cell. In fact there is no capacity decrease observed for the high temperature cell up to 1C cycling rate; only at 2C and 3C a slight reduction can be made out. For the RT cell, on the other hand, a clear step function behaviour can be observed. This underlines that rate capability of LNMO cathode material is enhanced at elevated temperature, probably due to increased ionic mobility. Nevertheless, it should be pointed out that the reversibility of the cell at higher temperature is lower than that at RT, not only during initial cycling where

the difference is most salient, but also during formation and rate capability and part of capacity retention testing. Only after approximately 50 cycles does the high temperature cell reach similar CE values as the RT cell. This lower reversibility is also reflected in the cycling stability, which continuously decreases for the HT cell while it remains stable at RT. Due to a cycler maintenance the HT cell was paused for two days and subsequently relaunched. The pause led to a noticeable loss in capacity. The lower capacity retention at elevated temperature compared to RT leads to intersecting capacities after approximately 80 cycles, which underlines that initial capacity gain is lost due to lower capacity retention in less than 100 cycles.

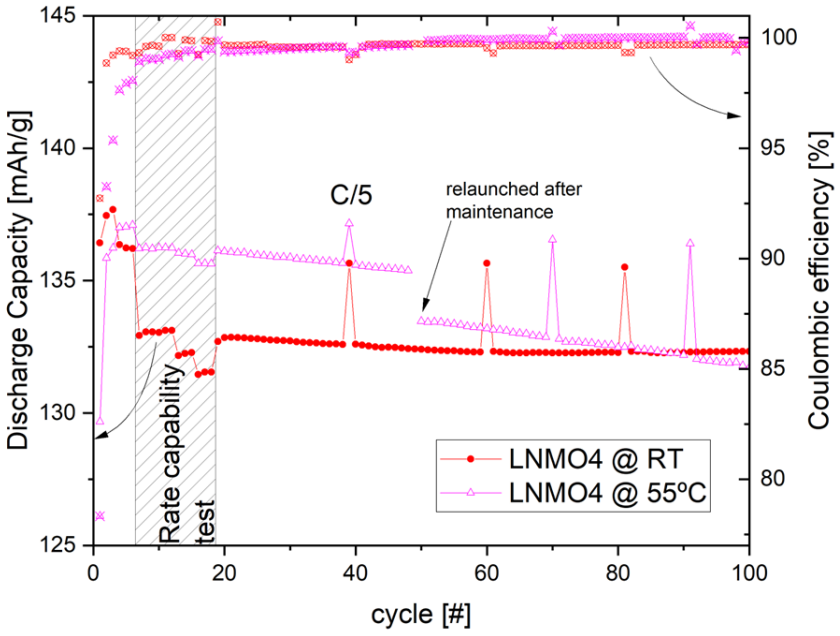

Figure 8: Rate capability and capacity retention test of LNMO cathode material half-cell at RT and elevated temperature of 55ºC.

4. Degradation analysis selection and processing of graphite and Si/C anode material

As pointed out in *D2.2 Final material data report and definition of final 3beLiEVe cell chemistry*, all Si/C candidates tested within this project show substantial capacity losses within the first 100 cycles when cycled in half cells vs Li with HVE already at slow cycling rate C/10 and C/5. Therefore, no additional rate capability tests were carried out on these materials. Interestingly, we find significant differences in the cycling performance and degradation rate of Si/C materials, although they have the same Si wt.% contents. To understand the phenomena that contribute to the degradation, the electrochemical signatures of the electrodes were studied, and post-mortem investigations were carried out. These are described in the following text.

4.1. Electrochemical analysis

The evolution of delithiation capacity of one of the provided Si/C candidates containing 15% Si in a half cell vs Li using HVE at C/10 is depicted in Figure 9. This anode material delivers almost 650 mAh/g in the first discharge, however after 100 cycles only 330 mAh/g are maintained. The initial coulombic efficiency (ICE) is about 66%, indicating that 1/3 of the inserted Li cannot be recovered. When limiting the lithiation capacity (depth of discharge (DOD)) to 550 mAh/g, the ICE increases to 87%, which means that much less lithium is irreversibly consumed. In subsequent cycles, almost all the inserted Li can be recovered with a CE >99%. After 45 cycles, the capacity limited electrode provides more reversible capacity than the non-limited electrode and continues to do so for more than 110 cycles. This exemplifies that limiting the lithiation capacity is an effective measure to enhance capacity retention of Si based electrodes in half cell configurations. In full cells, the limitation of DOD could be implemented via reducing the voltage window or via setting a capacity limit value during the lithiation.

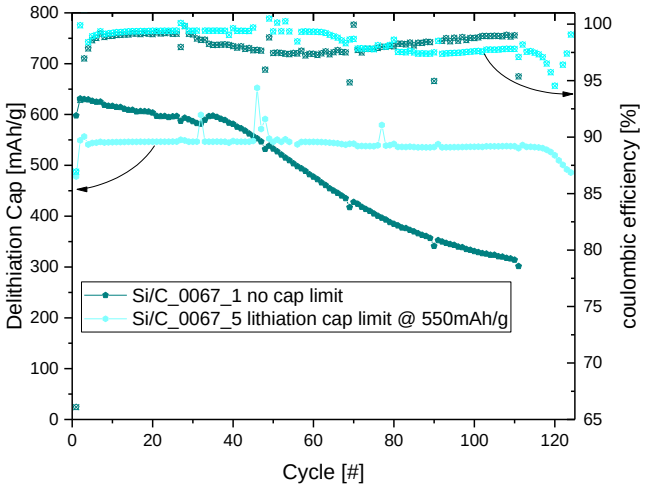

Figure 9 Reversible gravimetric capacity and corresponding coulombic efficiency for Si/C electrodes cycled in half-cell vs Li with and without lithiation capacity limitation.

To understand which impact the capacity limitation has on the lithiation mechanism of Si/C electrodes, the corresponding voltage capacity curves were examined, see Figure 10. For the lithiation without limitation (black solid line) the first lithiation (CC+CV) extends to almost 900 mAh/g with a sloping voltage profile around 0.07 V vs Li^+/ Li. In its second lithiation, the electrochemical signature is clearly distinct with much sloping profiles, reduced capacity, and an elevated share of capacity in the CV step. This suggests an

important growth of kinetic hindrance as well as loss of cyclable anode material (likely due to SEI formation and particle breakup). After 100 cycles (solid green line), we see further reduction of overall capacity in the CC step whereas the capacity in the CV step decreases less strongly. This leads to the fact that at the 100th cycle, about 30% of overall capacity originates from the CV step at 0.05V, whereas in the first cycle, less than 7 % of the total capacity falls within the CV step. This emphasizes the growth in overpotential upon cycling. For the Si/C electrode with lithiation capacity limit at 550 mAh/g (dashed lines), the changes in the lithiation profile are much less pronounced. However, an increase in overpotential can also be observed, resulting in a steeper voltage decay at capacities beyond 400 mAh/g. In this regard, it has been reported that the recrystallization of $Li_{3,75}Si$ exerts strong stresses on the material, leading to particle cracking and contact loss. We can hence conclude that limiting the lithiation capacity in half cells is an effective way to circumvent or at least delay this detrimental recrystallization resulting in a significant gain in capacity retention. This concept could be transferred to full cell level by limiting the Depth of Discharge (DoD) via capacitive or potential limitation.

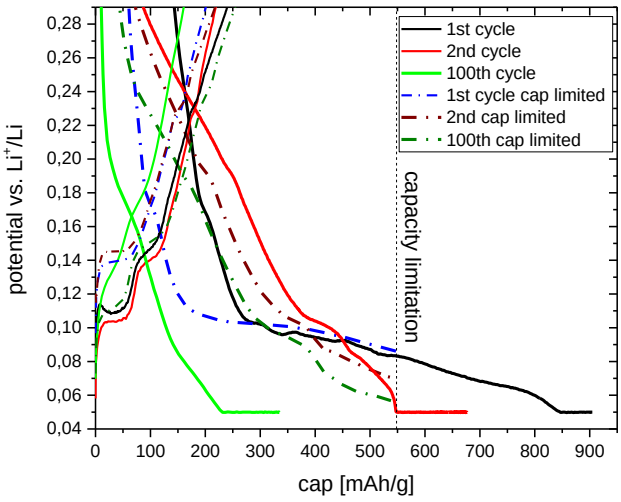

Figure 10 Voltage Capacity curves of 1st, 2nd and 100th cycle for Si/C half cell with (dashed lines) and without capacity limitation (solid lines)

4.2. Morphological analysis

SEM micrographs of pristine and cycled Si/C electrodes, which were investigated in half cells, are presented in Figure 11 left and right, respectively. Pristine electrode shows homogenous, primarily polygonal particles in the range of 5-20µm, which are decorated with smaller sub micrometre particles. In back scattered electron (BSE) images (not shown), the latter appear brighter than the graphite matrix which indicates elevated Si contents. Also a few scattered, spherical particles which are much brighter can be seen, thereby pointing towards the presence of isolated pure Si. After cycling (right hand side) the topography and morphology of the electrodes is clearly altered. The surface roughness has increased significantly due to the formation of larger blocks of up to 100µm and craters. These changes are testimony to the strong volume expansion and contraction that the Si/C electrode undergoes upon Li insertion and de-insertion. Despite the evident change in particle size distribution to the tens of micrometre scale, the decoration with sub micrometre particles can still be sparsely observed after cycling.

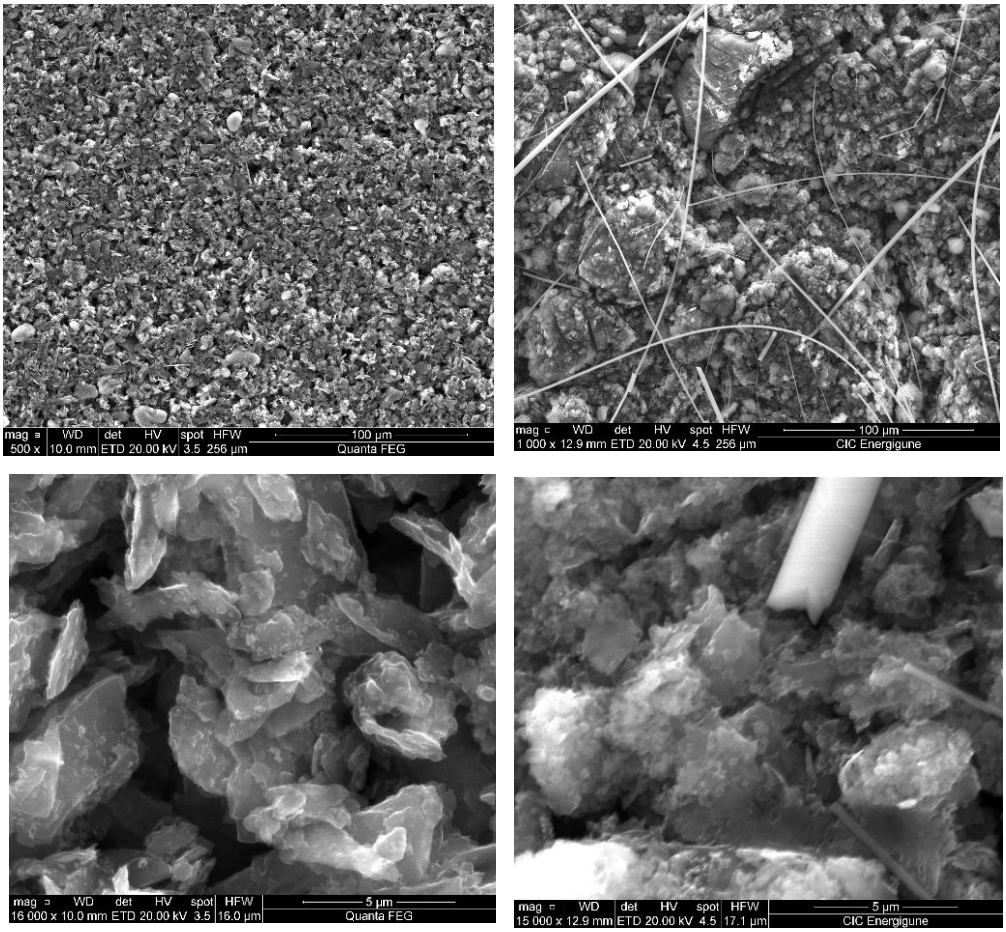

Figure 11 Micrographs of selected Si/C electrode before (left) and after cycling (right) in half cell vs Li. The rods on the cycled electrodes stem from the glass fiber separator.

5. Full-cell degradation analysis

While at half-cell level some irreversible reactions can be disguised by the unlimited supply of lithium and electrolyte in the cell, in the closed, full cell system even a minor irreversibility of less than one percent can lead to an accelerated capacity fade due to their cumulative nature. It is hence at full cell level where the consequences of undesired parasitic reactions are particularly detrimental and evident. In the following, selected degradation analysis on the LNMO//Si/C full cell using HVE are presented. Due to the excessive workload in WP2 task 2.3 and the resulting delay in the decision on the final cell chemistry, some of the characterization techniques have only been carried out on the LNMO//graphite system and not on the final 3beLiEVe cell chemistry. For the same reason, some of the testing originally foreseen at full cell level of the final cell chemistry within WP2, such as rate capability test, high temperature test and automotive use case test could not be included. Rate capability test was postponed to WP3 and will be included in *D3.3 Test report of influence of internal sensor on performance and degradation.* Automotive use case will be tested in task T7.1 *Testing of prototype cells with test protocol* and documented in *D7.1 Test report on prototype cells including baseline data*.

5.1. Electrochemical cycling analysis

The electrochemical signature and its evolution over cycle number contains a variety of insightful information on the reversibility of the redox reaction and its kinetic and thermodynamic interdependencies. The charge and discharge curves of LNMO//Si/C full cells using different electrolytes after 50, 120 and 250 cycles and their corresponding dQ/dV are depicted in Figure 12. One can clearly observe a shortening of the charge and discharge plateaus, as well as a decrease in dQ/dV, which indicates that the amount of charge interchanged between the cathode and anode decreases with growing cycle number. Furthermore, one can observe that the overpotential growth is more pronounced in electrolyte E than in C. Interestingly, the discharge (reduction) is more prone to suffer from overpotential growth than the charge (oxidation) reaction.

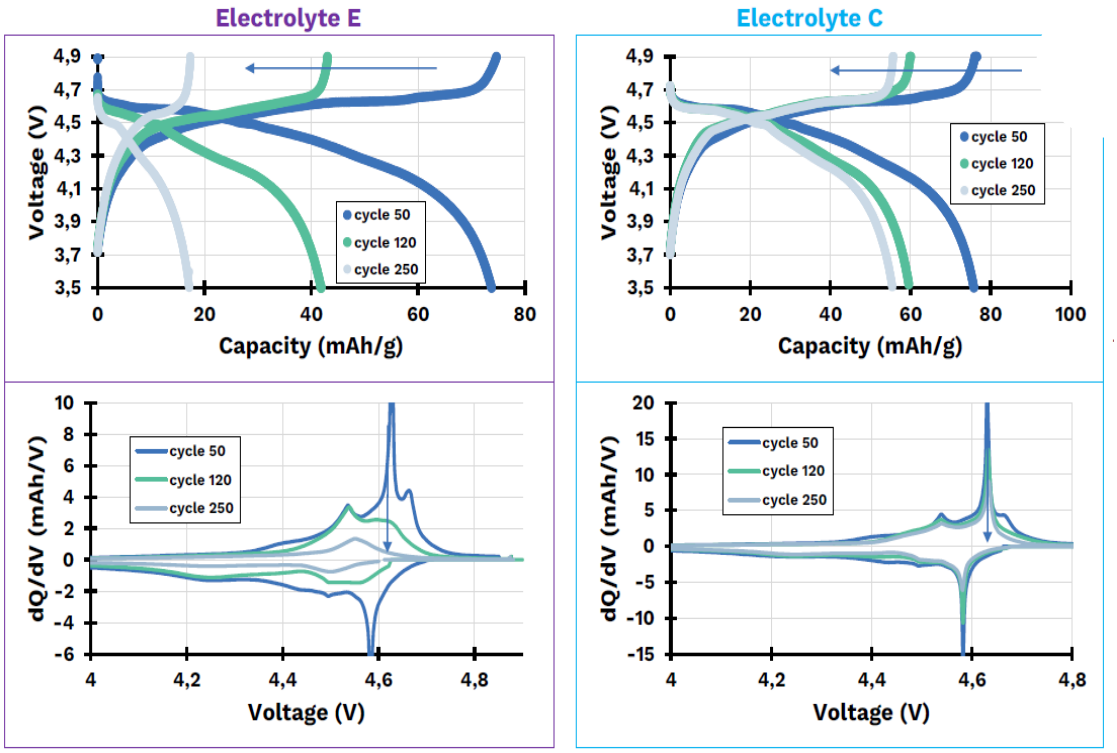

Figure 12 Top: capacity vs voltage and bottom: first derivative of charge vs voltage at 50, 120 and 250 cycles for LNMO//Si/C full cell coin cells using two different electrolytes E (left) and C (right)

To further investigate the electrochemical phenomena occurring in LNMO//Si/C full cell system, selected full cells, which were constructed and tested using the coin cell setup, were disassembled after several hundreds of cycles. The capacity as a function of cycle number of one of the test cells is depicted in Figure 13. The reversible capacity at begin of life (BoL) was ≈ 105 mAh/g and continuously fades upon cycling to reach about 44 mAh/g at C/5 after almost 300 cycles.

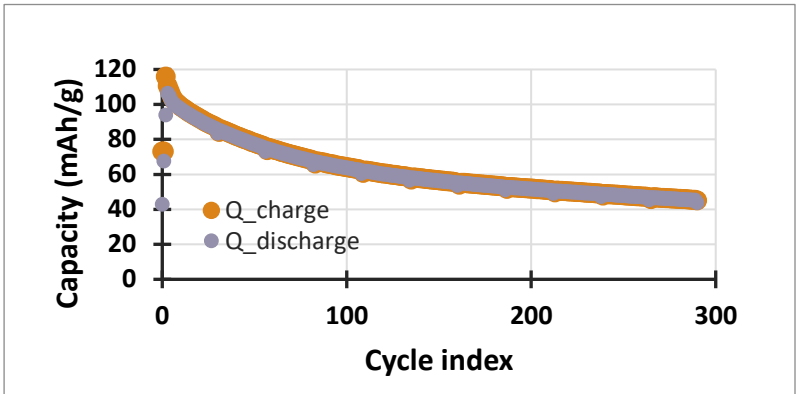

Figure 13 Specific gravimetric charge and discharge capacity of LNMO//Si/C full cell coin cell

To study the cycling capability of the anode and cathode individually, the discharged cell was disassembled and the LNMO and Si/C electrodes were reassembled in half cells with fresh electrolyte and Li metal as the counter electrode. As the first step, the Li inventory was measured for both electrodes. It was found that for the LNMO electrode, which is shown in Figure 14(top), although the full cell was stopped at complete discharge, Li could still be inserted, resulting in an initial discharge capacity of 73 mAh/g. This proves that the lithiation in the full cell was incomplete. Moreover, in the 2nd discharge cycle, this electrode provides a reversible capacity of 133 mAh/g, demonstrating that the LNMO electrode can deliver capacities close to BOL (135 mAh/g) after 300 cycles when sufficient cyclable Li and fresh electrolyte are supplied. This underlines our observation from the post-mortem that the LNMO electrode undergoes only minor degradation upon cycling and is hence not a critical driver for the observed capacity losses in the full cell system. The analysis of LNMO lithiation state also shows that at the EOC after 300 cycles, there was still ~16 mAh/g of lithium remaining in the cathode[1]. The fact that this capacity could not be extracted from the LNMO even when the full cell voltage reached 4.9V suggests that the LNMO delithiation was impaired by the overpotential that had built up during 300 cycles.

[1] 133-44-73 = 16 mAh/g. After 300 cycles, at the EOD, 44 mAh/g of Li were inserted in the cathode. Then in the half cell, an additional 73 mAh/g of Li were inserted in the cathode, and 133 mAh/g were subsequently extracted, meaning that there was initially (at the EOC after 300 cycles) 16 mAh/g of Li "kinetically blocked" in the LNMO.

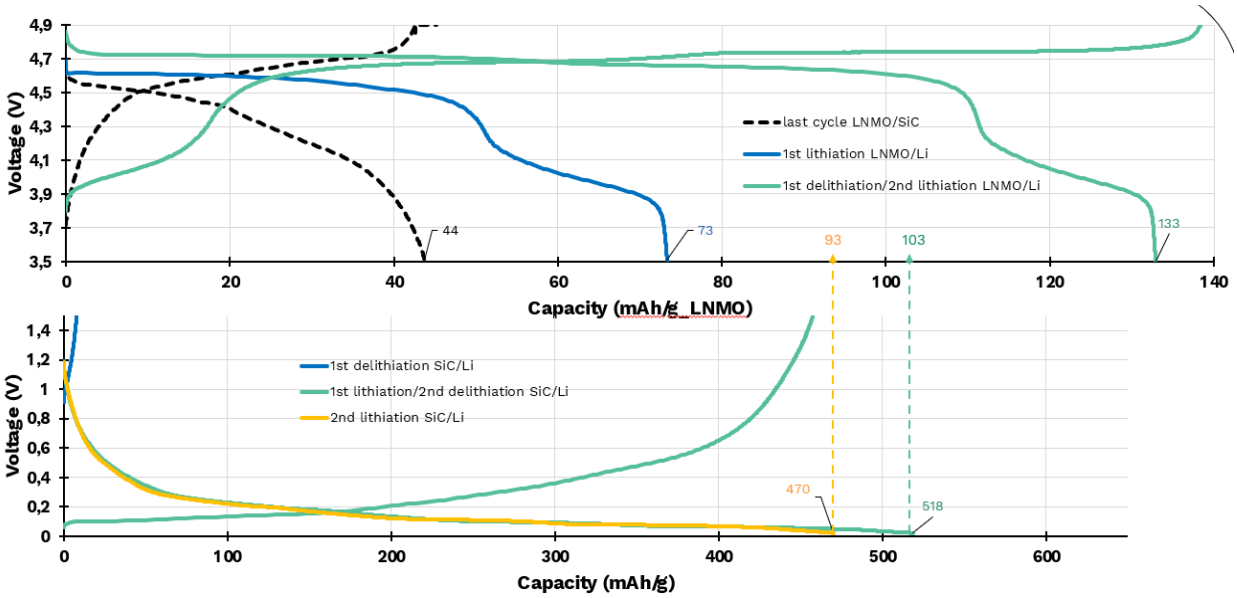

Figure 14 Voltage vs Capacity curves for recovered LNMO (top) and Si/C electrode in half cell vs Li at C/10. The dashed line in top graph corresponds to last cycle of the full cell before disassembly after almost 300 cycles.

For the Si/C electrode Figure 14 (bottom) the Li inventory analysis revealed only a small quantity of (2 mAh/g$_{_LNMO}$) remained in the Si/C electrode at EOD in the full cell. Similar to LNMO, the reason for the incomplete delithiation of the Si/C could be due to the build-up of kinetic hindrance in the discharge reaction, which pushes part of the effective Si delithiation potential beyond the upper cut-off voltage. When lithiating the Si/C electrode in a fresh half cell, a value of 518 mAh/g was achieved, of which 457 could be recovered in subsequent delithiation. This corresponds to 83% of the initial reversible capacity of 550mAh/g.

Interestingly, the second lithiation of Si/C dropped to 470 mAh/g. Since in the half cell both Li and electrolyte are abundant, this decrease is most likely due to the SEI formation which leads to an increased overpotential on lithiation due to the resistance of the SEI layer. Therefore, a lower potential has to be achieved in order to overcome the overpotential and further lithiate the Si/C electrode.

Summing up the combined Li inventory of both electrodes, we find that 91mAh/g$_{_LNMO}$[2] of Li capacity has been lost for the reversible cycling after 300 cycles. A small part of this loss (20%) was kinetically blocked in the electrodes, particularly in the cathode, most likely due to overpotential build-up as a consequence of charge transfer resistances. Another degradation contribution (also around 20%) stems from the degradation of the electrodes, in this case particularly on the anode side, which is consistent with the visual inspection of the electrodes and SEM analysis (sections 4.2 and 4.5). However, most of the capacity fade (>60%) is due to the irreversible consumption of lithium. Since this Li can neither be extracted from the anode nor from the cathode it must have irreversibly reacted to thermodynamically more stable compounds such as LiF or Li_2CO_3 in the SEI, which is supported by the EIS analysis showing the constant growth of the SEI layer.

A summary of the different contributions to the overall observed capacity loss is depicted in the pie chart in Figure 15. It should be noted that some of the lost capacity can be the result of multiple overlapping effects which cannot be accurately expressed in this pie chart. The values given here can hence only provide a simplified and incomplete picture of the complex degradational mechanism.

[2] 135 – 44 = 91 mAh/g. 135mAh/g is the theoretical reversible capacity of LNMO cathode while 44 mAh/g is the reversible capacity achieved after 300 cycles in the full cell.

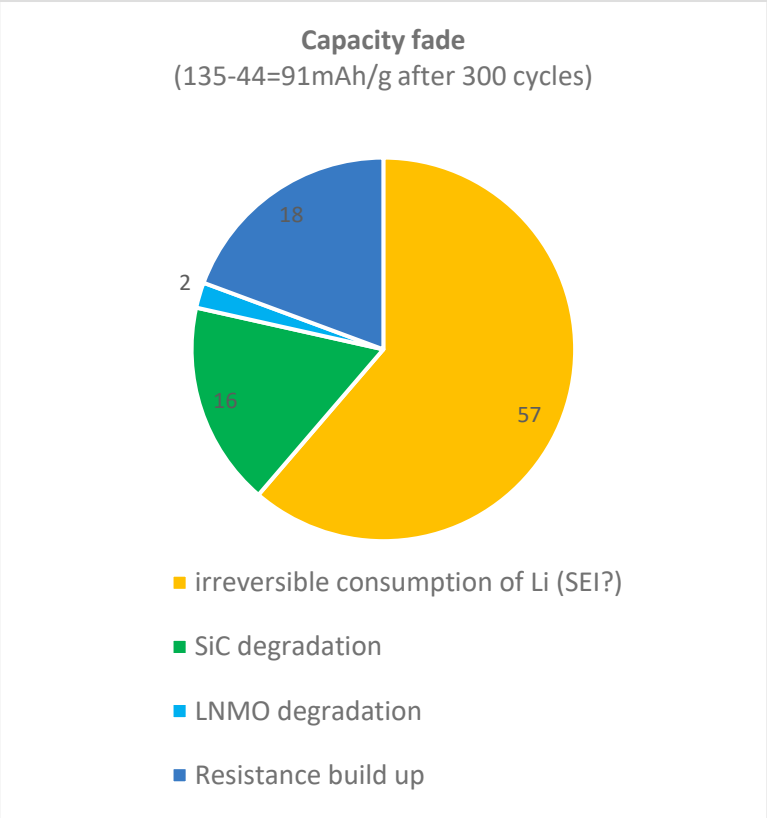

Figure 15: Pie chart showing a simplified overview of the main contributions to the overall observed capacity loss. Due to cross degradational effects absolute values should be taken with due care.

5.2. FIB-SEM

Focused ion beam scanning electron microscopy (FIB-SEM) was conducted on pristine and cycled electrodes of LNMO//Graphite and LNMO//Si/C cells and are depicted in Figure 17 and Figure 16, respectively. For the cycled LNMO in the LNMO//Graphite cells, we observe no significant changes in the particle size however we observe a change in the appearance of the surface such as smoothing, which suggests a LNMO surface modification upon cycling. Since the CEI is expected to be in nm scale, it is unlikely that it is the dominant phenomenon in these micrographs. The depth profile of the graphite counter electrode reveals voids in the graphite electrode before and after cycling, suggesting that the electrode densification was not at optimum.

For the LNMO/Si/C electrode depicted in Figure 16, we observe dense electrode in the depth profile of LNMO before and after electrochemical cycling. No evident structural changes upon cycling are detected. The elemental analysis on this electrode reveals besides the expected TM-O, the presence of F and P from electrolyte as well as traces of Si. The Si/C electrode is more porous than the LNMO electrode but no increase in porosity can be determined based on FIB SEM. A surface smoothing is observed, which could be related in part to the SEI formation as well as the irreversible transformation of crystalline to amorphous Si. Analogous to the cathode, the elemental analysis of the Si/C anode shows F and P which can be attributed to the electrolyte as well as Mn stemming from the cross-talk in line with results from XPS analysis, see Figure 4.

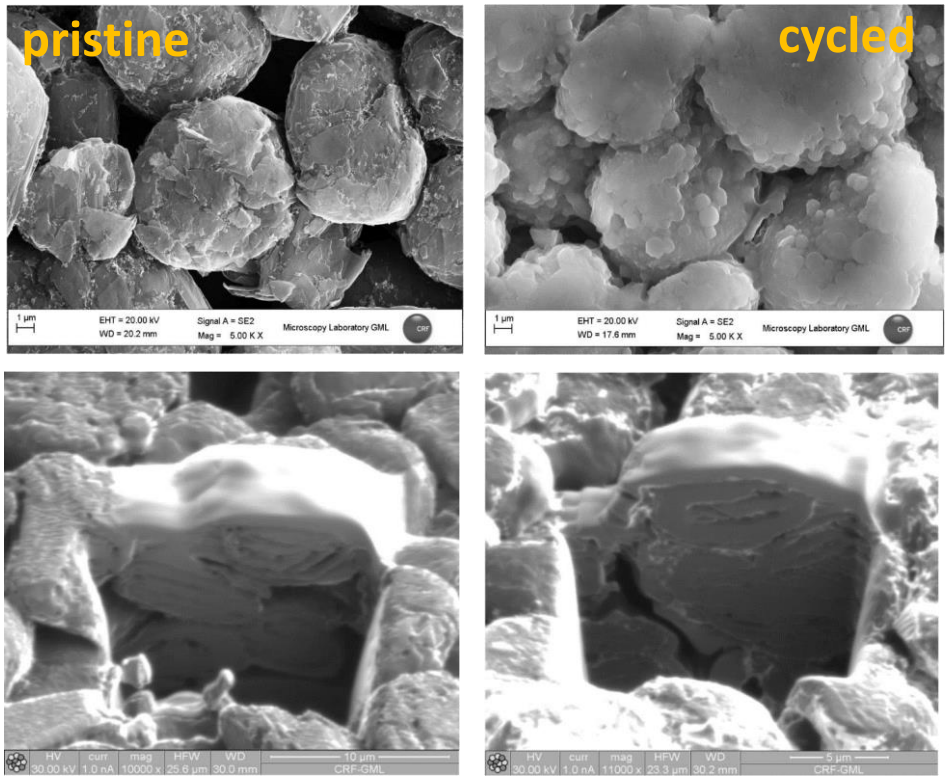

Figure 17 SEM micrographs of Top: LNMO electrode before (left) and after cycling (right), bottom FIB-SEM micrographs of pure graphite electrode before (left) and after cycling (right)

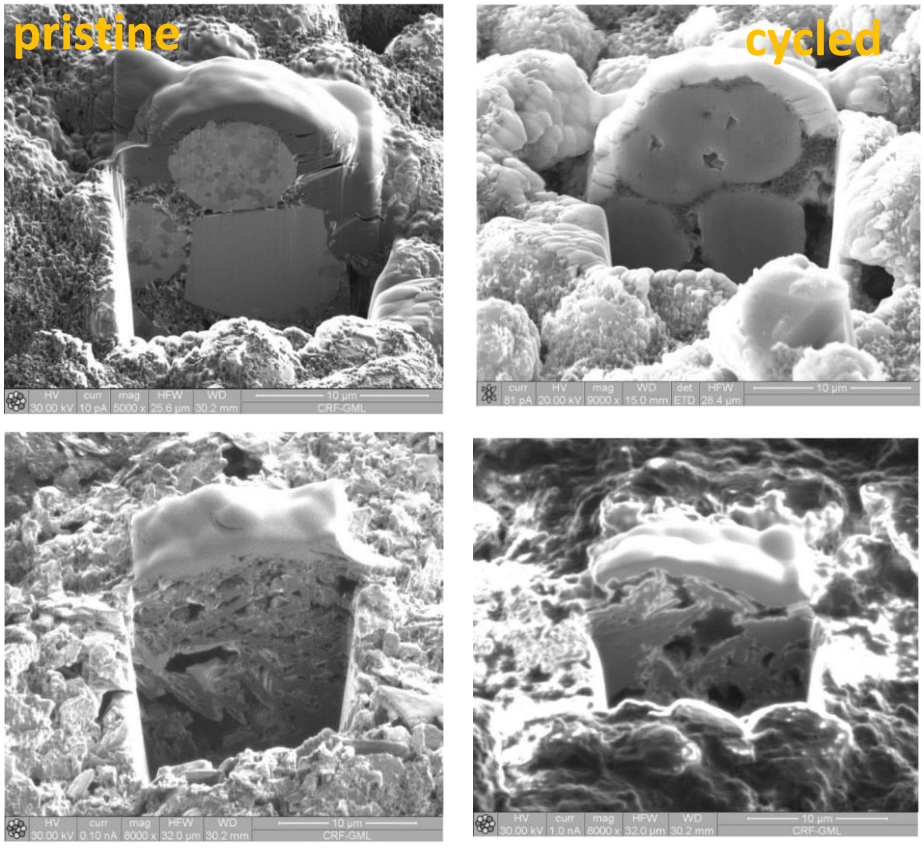

Figure 16 FIB SEM micrographs of Top: LNMO electrode before (left) and after cycling (right), bottom: Si/C electrode before (left) and after cycling (right)

5.3. Raman Spectroscopy

Raman spectroscopy was performed on electrodes from disassembled full cells using the two different electrolytes. The spectrum of Si/C of cycled electrode is compared to pristine electrode in Figure 18. This comparison reveals the disappearance of the sharp peak at 519 cm^{-1} and the appearance of a broad feature centred around 470 cm^{-1}. This can be attributed to the irreversible transformation from crystalline Si to amorphous Si upon first lithiation and delithiation. The features attributed to graphite, which are the D, G and overtone 2D bands at 1348, 1583 and 2712 cm^{-1}, respectively, undergo no major changes upon electrochemical cycling. We observe a slight increase in the D/G band ratio upon cycling, which can be interpreted as an increase in disorder and defect concentration upon electrochemical cycling in the graphite. These effects are accompanied by a slight shift of the D and 2D bands to higher wavenumbers for the cycled electrode. This red shift suggests a reduction of the average C–C bond strength which might be related to increased defects.

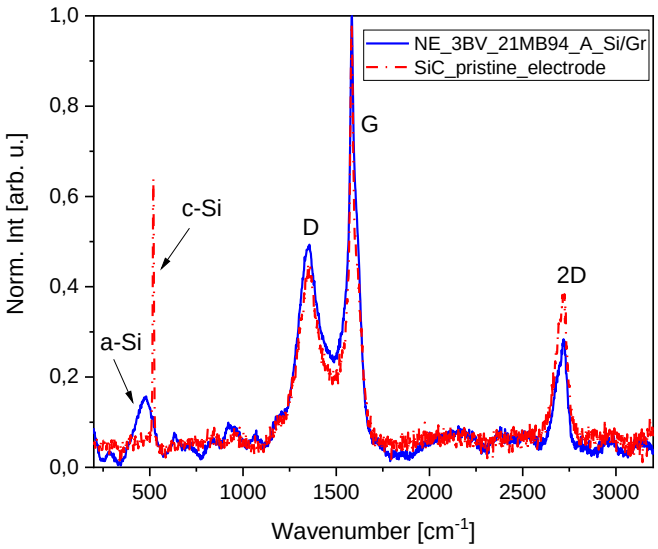

Figure 18 Raman spectra of pristine and cycled Si/C electrode.

The Raman spectra of LNMO cathode of that cell is depicted in Figure 19. Unlike the spectra of cycled LNMO taken from half-cells presented in Figure 3, we observe strong spectral changes for the cycled LNMO from the full cell particularly for the main part of the recovered LNMO electrode (lower part). All new features in its spectrum can be attributed to charged states of LNMO such as the emerging peak at 550 cm^{-1}, which can be attributed to the presence of Ni^{4+}. This comes as a surprise as at the end of discharge, complete re-lithiation of the LNMO electrode should be achieved and all Ni should be in its reduced form Ni^{2+} exclusively. The fact that this is not the case highlights that the re-lithiation reaction is incomplete. This is well in line with the observation made in section 5.1 and underlines the hypothesis that there is a lack of cyclable Li in the system to re-lithiate the LNMO. The spectral differences between the main electrode (lower part) and a thinner layer stuck on the separator (upper part) suggests a gradient of re-lithiation as a function of depth of electrode. The electrode part closest to the separator is more lithiated and its spectra hence resembles that of pristine LNMO much more than that of the deeper LNMO.

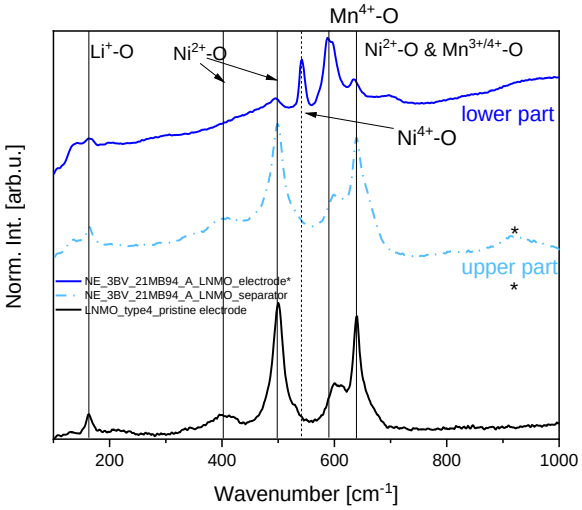

Figure 19 Raman spectra of cycled and pristine LNMO cathode. Upon disassembly part of the LNMO was stuck on the separator and could not be removed, it is here referred to as "upper part"

5.4. EIS

Electrochemical impedance spectroscopy (EIS) allows the electrical response of the complex battery system to be decoupled into its individual contributions of bulk anode, cathode, electrolyte, and their respective interfaces. This is done by measuring the frequency dependence of the impedance of a battery and subsequently fitting the result with an appropriate model (equivalent circuit). Moreover, this method can be performed under *in situ* conditions at distinct SOC without disassembling or harming the cell. Despite these assets, EIS has its challenges and pitfalls which will not be addressed in detail here. Furthermore, due to its incompatibility with stainless steel environment, the selected HVE could not be used in this specially designed PAT-Cell. The results should hence be taken with a grain of salt. The evolution of impedance during the first 45 electrochemical cycles of the complete cell, the LNMO cathode and the graphite anode are depicted in Figure 20 from left to right. Top row are the Nyquist plots and bottom row the corresponding Bode plots.

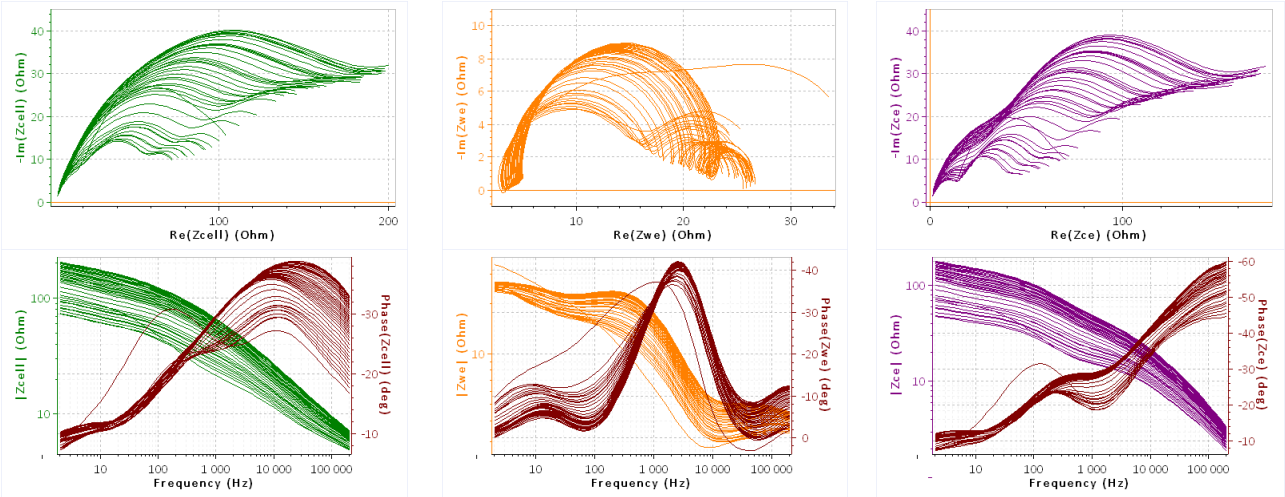

Figure 20: Nyquist (top) and Bode (bottom) plot evolution during first 45 electrochemical cycles of complete cell (left), LNMO cathode (centre) and graphite anode (right).

A simple comparison of the Nyquist plots of the complete cell with those of the anode and cathode reveals that the complete cell resembles much more the response of the anode than that of the cathode. This

suggests that the overall impedance is dominated by the anode. Throughout equivalent circuit fitting, these contributions can be further deconvoluted. In the model applied, three interfaces were included for the anode to adequately fit the data set. These correspond to the current collector/ electrode (R2), the electrode/ SEI (R3) and a third interface (R4), while R1 corresponds to serial resistance. In Figure 21, the evolution of selected resistances upon cycling from both anode (violet outline) and cathode (orange outline) are compared.

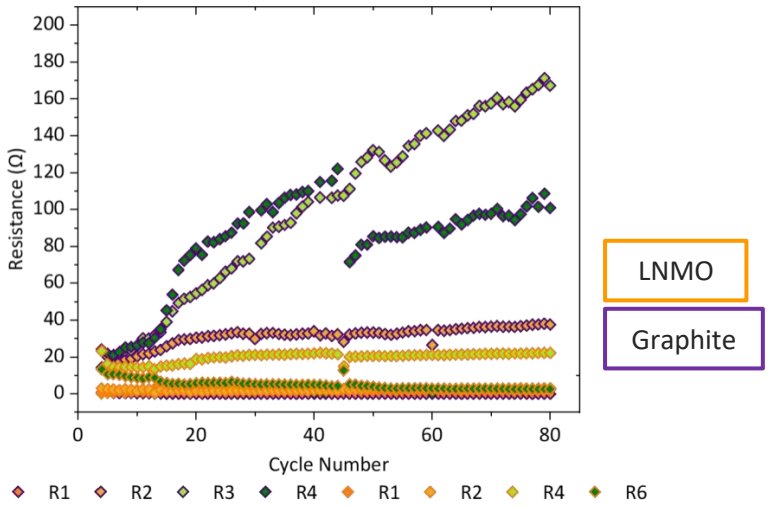

Figure 21 Evolution of resistances related to LNMO cathode (orange outline) and Graphite anode (violet outline) as function of cycle number in a LNMO//Graphite full cell.

The graph clearly illustrates that the resistance that is increasing the most upon electrochemical cycling is the interfacial SEI related resistances at the graphite anode R3, which reflects the formation and continuous growth of the SEI. The second strongest growth can also be attributed to a graphite related interface R4. Although its origin is still speculative, the fact that after cell resting after 45 cycles, a strong drop is observed after which it continues to rise upon further cycling bears resemblance to a slow diffusion dominated process such as the Li migration from the electrolyte into SEI. The third although much less pronounced increase can also be attributed to the graphite electrode R2, which represents the current collector/ electrode interface. The increase in the first 15 cycles followed by a slower increase suggest a reduction of charge mobility at this interface likely due to volume change of the graphite host structure upon Li uptake and release. On the cathode side (orange outline) the only noticeable increasing resistance observed is the CEI related R4. Nevertheless, it shows only a minor increase during the first 20 cycles and then stabilizes. Neither for the current collector/ electrode resistance (R6) nor for R2 were there any noticeable changes observed on the cathode side. This comparison underlines that the main resistive build up occurring upon cycling of LNMO // graphite full cell occurs at the anode via the SEI formation. Although the formation of SEI is pivotal for the reversible functioning of carbonaceous electrode, the continuous increase in resistance observed in EIS infers irreversible Li consumption and hinders the Li ion migration which are detrimental for cycling performance.

4.5 Visual inspection of disassembled pouch cell

Figure 22 shows photographs of the cell components (cathode, anode, and separator) after cycling the following full cell monolayer pouch cells:

1) LNMO4/Graphite(CCI)/HVE-A ; discharged 3.5 V; 140 cycles
2) LNMO4/SiC-164/HVE-A; discharged 3.5 V; 160 cycles

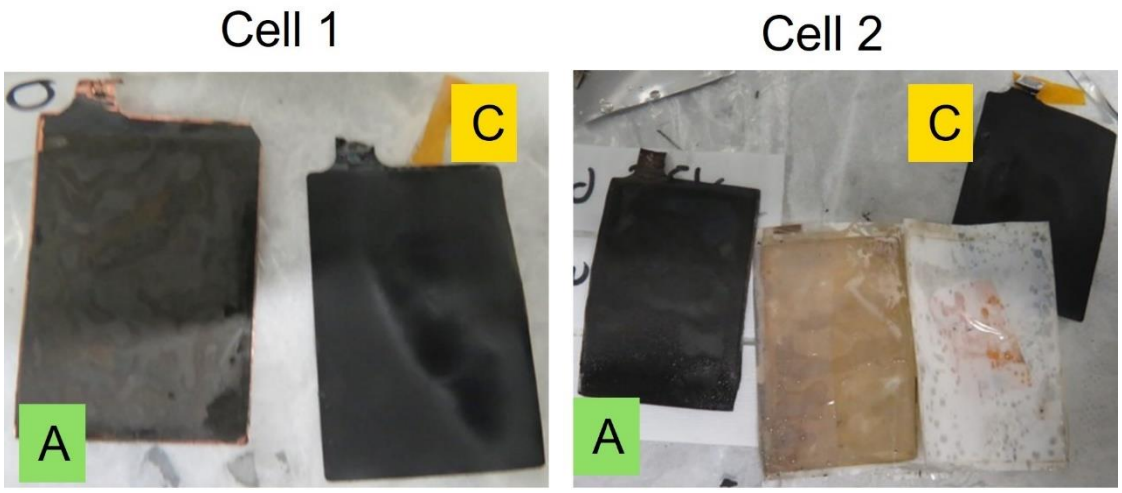

Figure 22 Photographs of the cell components after cycling. A = anode, C = cathode.

Irrespective of the cell chemistry, it can be noticed that the LNMO4 cathode is in very good condition after cycling and no material detachment nor inhomogeneities were observed. However, the anodes of both cells showed delamination from the edges. The separator was not damaged (not shown for cell 1). However, it can be seen that the separator of cell 2 has material from the negative electrode somewhat dissolved on it (brownish colour). This was not noticed for cell 1. This could be attributed to the higher intrinsic stress of the Si/C material, and it can be suggested that the binder distribution along the electrode is insufficient, leading to low electrode adhesion and thus active material dissolution. This underlines the need for additional effort in optimization of electrode formulation and processing. Regarding the wetting of the cell, electrolyte dry-out phenomena was not observed in any of the cells.

4.6 Gas chromatography - mass spectrometry

GC-MS measurements were performed on the pristine electrolyte as well as of aged electrolytes of both cells (presented in previous sections) to gain further insight on their stability, see Figure 23. The main peaks identified for the pristine and cycled electrolyte are EMC with a retention time of 3.4 min, EC with a retention time of 6.1 min, and FEC with a retention time of 5.2 min. Slight fluctuations in peak intensities are attributed to sample preparation and handling, as compounds such as EMC are very volatile. However, since the main peaks of the aforementioned compounds are still visible after cycling and no new compounds are present, it can be assumed that the general electrolyte composition (solvent, co-solvents and additives) is maintained after 160 cycles regardless of the use of graphite or Si/C as anode. The fact that no degradational products are detected despite the strong evidence of parasitic side reactions (XPS, XAS, EIS) can be explained by the insolubility of the degradation products or by their concentrations lying being below the detection limit. It should be noted that no significant gas evolution was observed on monolayer pouch cell level.

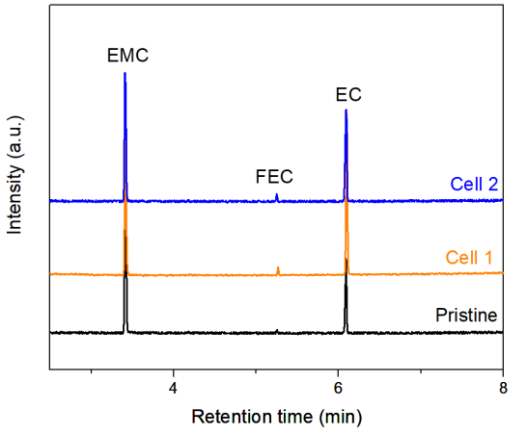

Figure 23 GC-MS analysis of the HVE-A electrolyte: pristine (black), aged electrolyte recovered from cell 1 (orange), aged electrolyte recovered from cell 2 (blue).

6. Conclusions

The stability of LNMO high voltage material upon electrochemical cycling was confirmed in both half cell and full cell systems via diverse techniques probing its long- and short-range structure, microstructure, and composition. The dissolution of both TMs and their shuttling to and deposition on the anode was detected via XPS and confirmed via EDX. However, it does not seem to be a critical driver of capacity deterioration. We found that the ratio of the TM deposited on the anode corresponds approximately to their stoichiometries in LNMO, which refutes the theory of preferential dissolution of Mn. Moreover, we found evidence that the dissolution process seems to be most prominent in the first cycle and then saturates upon further cycling. The occurrence of parasitic reactions at elevated potentials during charge has been rendered visible via operando XAS. This tendency is further increased when cycling at elevated temperature, highlighting the need for developing electrolytes with extended oxidative stability window. For the Si/C anode material, profound structural and morphological changes upon electrochemical cycling such as the conversion from crystalline to amorphous Si were observed. Considering the severe capacity fading observed for the high-Si anode candidates, we have demonstrated that limiting the lithiation capacity can cushion the stress related to recrystallization of lithiated phases, thereby enhancing cycle life. It is hence expected that limiting the DoD on full cell level would lead to a significant gain in cycling stability for this cell chemistry.

In the full cell investigations, the irreversible consumption of lithium in the SEI and the resulting lack of cyclable Li as well as the resulting resistive build-up were identified as the main drivers of capacity fade, while the electrode deterioration plays a secondary role. In fact, considering the capacity loss when reassembling cycled LNMO electrodes in fresh half-cells, the degradation was found to be negligible. Although the degradation was more pronounced for the Si/C electrode, most of the lost capacity could be recovered when paired with fresh electrolyte and replenished lithium reservoir. The non-recoverable capacity loss found for Si/C could be due to the loss of electrical contact of particles upon expansion and shrinkage, resulting in detachment and dissolution in the electrolyte as shown by the post-mortem inspection, e.g., colouring of the electrolyte. Interestingly, it was found that the general composition of HVE was maintained over cycling and no soluble degradation by-products or significant gas evolution were detected.

Consequently, future work should focus on managing the lithium household within the cell, assuring the availability of sufficient lithium to re-lithiate the cathode even after extended cycles. This can be achieved via adequately adjusting the N/P ratio but also via less conventional methods such as pre-lithiation of anode, designing lithium excess cathode materials as well as introducing a lithium reservoir in the electrolyte. One of the principal challenges for the here investigated LNMO// Si/C cell chemistry is to form a thin but functional SEI, protecting the anode from solvent co-intercalation while at the same time allowing for fast Li ion exchange and avoiding irreversible Li consumption. Furthermore, the importance of electrode formulation (e.g., binder selection) and processing for the Si/C anode has been highlighted. These are crucial to ensure electrode integrity and electrical contact of active material particles despite elevated stress levels upon electrochemical cycling.

Due to the excess workload in WP2 and the resulting delay, the rate capability test and high temperature test could not be applied on final cell chemistry. The rate capability testing was hence postponed into WP3 and will be included in *D3.3 Test report of influence of internal sensor on performance and degradation*. We are looking forward to continuing the degradational analysis on full cells at scale of 30Ah pouch in WP7 task 7.1.

This project has received funding from the European Union's H2020 research and innovation programme under Grant Agreement no. 875033.

This publication reflects only the author's view and the Innovation and Networks Executive Agency (INEA) is not responsible for any use that may be made of the information it contains.